Piezoelectric Sensors Operating at Very High Temperatures and in Extreme Environments Made of Flexible Ultrawide-Bandgap Single-Crystalline AlN Thin Films

Nam-In Kim, Miad Yarali, Mina Moradnia, Muhammad Aqib, Che-Hao Liao, Feras AlQatari, Mingtao Nong, Xiaohang Li, and Jae-Hyun Ryou*

Extreme environments are often faced in energy, transportation, aerospace, and defense applications and pose a technical challenge in sensing. Piezoelectric sensor based on single-crystalline AlN transducers is developed to address this challenge. The pressure sensor shows high sensitivities of 0.4–0.5 mV per psi up to 900 °C and output voltages from 73.3 to 143.2 mV for input gas pressure range of 50 to 200 psi at 800 °C. The sensitivity and output voltage also exhibit the dependence on temperature due to two origins. A decrease in elastic modulus (Young's modulus) of the diaphragm slightly enhances the sensitivity and the generation of free carriers degrades the voltage output beyond 800 °C, which also matches with theoretical estimation. The performance characteristics of the sensor are also compared with polycrystalline AlN and single-crystalline GaN thin films to investigate the importance of single crystallinity on the piezoelectric effect and bandgap energy-related free carrier generation in piezoelectric devices for high-temperature operation. The operation of the sensor at 900 °C is amongst the highest for pressure sensors and the inherent properties of AlN including chemical and thermal stability and radiation resistance indicate this approach offers a new solution for sensing in extreme environments.

1. Introduction

Accurate, reliable, and robust sensing of physical and mechanical parameters such as pressure, force, strain, deflection, deformation, and acceleration is the crucial input for the control and integrity of systems. While the sensing and monitoring of such parameters are routinely carried out at near-room temperatures and in general ambient conditions, it becomes very challenging in applications that require operation in extreme environments such as high temperatures, exposure to corrosive media and radiation, and mechanical vibration. Current and next-generation energy, transportation, and defense applications demand pressure, strain, and vibration sensing in extreme conditions, including combustion engines, gas turbines, aerospace propulsion, deep oil drilling, nuclear power, geothermal energy, chemical plants, and high-pressure hydrogen storage. The majority of them require operation at very high temperatures along with other harsh conditions such as compressor and exhaust of gas turbine (400–650 °C), deep geothermal wells (450–600 °C), various nuclear reactors from light water to high-temperature reactors (300–1000 °C), aerospace turbomachinery (75–500 °C) as well as in the petrochemical industry where pipeline pressures must be monitored at various climates ranging from desert heat to near arctic cold.[1] Highly sensitive, reliable, and durable sensors that can tolerate such extreme environments are necessary for the

N.-I. Kim, M. Yarali, M. Moradnia, M. Aqib, J.-H. Ryou
Department of Mechanical Engineering
University of Houston
Houston, TX 77204-2004, USA
E-mail: jryou@uh.edu

N.-I. Kim, M. Yarali, J.-H. Ryou
Materials Science and Engineering Program
University of Houston
Houston, TX 77204, USA

N.-I. Kim, M. Yarali, M. Moradnia, M. Aqib, J.-H. Ryou
Advanced Manufacturing Institute (AMI)
University of Houston
Houston, TX 77204, USA

N.-I. Kim, M. Yarali, M. Moradnia, M. Aqib, J.-H. Ryou
Texas Center for Superconductivity at UH (TcSUH)
University of Houston
Houston, TX 77204, USA

C.-H. Liao, F. AlQatari, M. Nong, X. Li
Advanced Semiconductor Laboratory, Electrical
and Computer Engineering Program
King Abdullah University of Science and Technology (KAUST)
Thuwal 23955, Saudi Arabia

J.-H. Ryou
Department of Electrical and Computer Engineering
University of Houston
Houston, TX 77494, USA

The ORCID identification number(s) for the author(s) of this article can be found under https://doi.org/10.1002/adfm.202212538.

**ADVANCED
SCIENCE NEWS**

www.advancedsciencenews.com

**ADVANCED
FUNCTIONAL
MATERIALS**

www.afm-journal.de

efficiency, maintenance, and integrity of the aforementioned applications.

Different techniques have been studied for the measurement of pressure and other physical parameters at high temperatures. Piezoresistive sensors using SiC were investigated to monitor the pressure of an internal combustion engine at temperatures above 300 °C.[2] However, the accuracy of the sensor is reduced as the temperature rises due to its lower resistivity and unstable metal/semiconductor contact.[3] SiC-based capacitive sensors showed poor resilience and were highly impacted by parasitic capacitance at high temperatures.[4] Another high-temperature pressure sensing technology is fiber optic sensors which are widely used because of their robustness, high operating temperature, and stability in corrosive environments; however, this type of sensor needs specific packaging to preserve the mechanically delicate fiber wires and fiber tips, in which sensor's mechanical failure may occur at high temperature due to thermal expansion coefficient mismatch between fiber and packaging materials.[5] It is necessary to develop a new approach to solve the existing problems associated with high-temperature sensors operating in harsh conditions.

Sensing based on piezoelectric transducers offers the advantages of simple structure, robustness, insensitivity to electromagnetic radiation, fast response time, and low-power consumption over other sensing mechanisms.[6] However, their implementation is limited by the operating temperature governed by their intrinsic property of Curie temperature. For high-temperature applications, several piezoelectric materials have been investigated including quartz (SiO_2), lithium niobate ($LiNbO_3$, LN), langasite ($La_3Ga_5SiO_{14}$, LGS), and gallium orthophosphate ($GaPO_4$) with all having different limitations (Table S1, Supporting Information). Quartz sensors suffer from low piezoelectric coefficients (hence low electromechanical coupling factors), the phase transition from α to β phase at ≈573 °C (causing a significant volume change), and performance deterioration above 350 °C.[7] The operation of LN sensors is limited by the depletion of oxygen to the ambient, inadequate resistivity, and chemical decomposition above 300 °C resulting in a short lifetime at high temperatures.[8] The sensing capability of LGS and $GaPO_4$ sensors at elevated temperatures are also limited by oxygen vacancies transport and diffusion in the lattice as well as lower mechanical quality as a result of higher structural disorder, respectively.[9]

Group III-nitride (III-N) wide-bandgap semiconductor materials ($Al_xGa_{1-x}N$) have the potential to overcome the current challenges in high-temperature piezoelectric materials in harsh environments. III-N materials have spontaneous and piezoelectric polarization and no solid-phase transformation at high temperatures; hence practically no Curie temperature.[10] They are also thermally stable, chemically inert, mechanically hard, and radiation hardened, which makes them inherently suitable for extreme-environment applications.[11] They are even biocompatible for selected biomedical applications such as pressure monitoring in blood vessels and abdominal aortic aneurysm.[12] The piezoelectric coefficients of III-N materials are not as high as those of lead titanate zirconate ($Pb[Zr_xTi_{1-x}]O_3$, PZT). However, electromechanical coupling factor (k_t^2) and mechanical to electrical energy conversion efficiency (η_{me}) of single-crystalline

III-N materials are sufficiently high thanks to their low dielectric constants:[13]

$$k_t^2 = \frac{e^2}{\varepsilon c} \tag{1}$$

$$\eta_{me} = \frac{\bar{e}^2}{\bar{k}E} \tag{2}$$

where e is piezoelectric coefficient, ε is dielectric constant, c is elastic stiffness constant, and $\bar{e}$, $\bar{k}$, and E are effective piezoelectric coefficient, effective dielectric permittivity, and elastic modulus, respectively.

We previously developed III-N piezoelectric pressure sensor using single-crystalline GaN thin films for harsh-environment applications.[14] We demonstrated a working sensor operating at high pressures; however, the sensitivity of the sensor starts decreasing at temperatures higher than 300 °C, which is not high enough for many harsh-environment applications. The temperature limitation is believed to originate from the bandgap energy of GaN (E_g = 3.4 eV). AlN (E_g = 6.2 eV), as the widest bandgap piezoelectric material, can overcome the limitation. Therefore, in the present study, we develop piezoelectric pressure sensors using AlN thin films. We also study the difference in the performance characteristics between GaN and AlN sensors by experimental characterization and numerical modeling to test the hypothesis of sensitivity degradation by bandgap energy.

2. Results and Discussion

2.1. Design of Flexible Sensor and Sensor Module

Figure 1 schematically illustrates the steps of the fabrication process of a sensor. First, we deposited chromium (Cr) and gold (Au) with thicknesses of 10 and 100 nm as an adhesion layer and an electrode, respectively, were deposited on III-N thin film via electron beam (e-beam) evaporation. Then, a thick layer of copper (Cu) (≈100 µm) was deposited electrochemically to serve as a flexible mechanical supporting layer. The electrodeposition was conducted at a current density of 0.04 A cm^{-2} with 1.1 V in 0.1 M of $CuSO_4$ electrolyte with Cu foil as a counter electrode. The Silicon (Si) substrate needs to be removed to endow the sensor structure with mechanical flexibility. Au with 100 nm of thickness was deposited on Cu to prevent Cu from damaging during Si wet etching, and then a sapphire substrate was glued to the opposite side of the Si substrate to serve as a handling substrate during the etching. A mixture of hydrofluoric (HF) acid (49%, Macron fine chemicals), acetic acid (50%, Macron fine chemicals), and nitric acid (70%, Fisher Chemical) was used, with volumetric ratios of 0.80, 0.15, and 0.05, respectively, for etching. After the Si removal, Cr/Au (10/100 nm) were deposited to sandwich III-N layer between two electrodes. Finally, the sapphire substrate was detached by acetone followed by isopropyl alcohol. The sensor is now mechanically flexible enough to be bent (Figure S1, Supporting Information).

Figure 2a schematically shows the structure of a pressure sensor module, consisting of a III-N thin-film piezoelectric
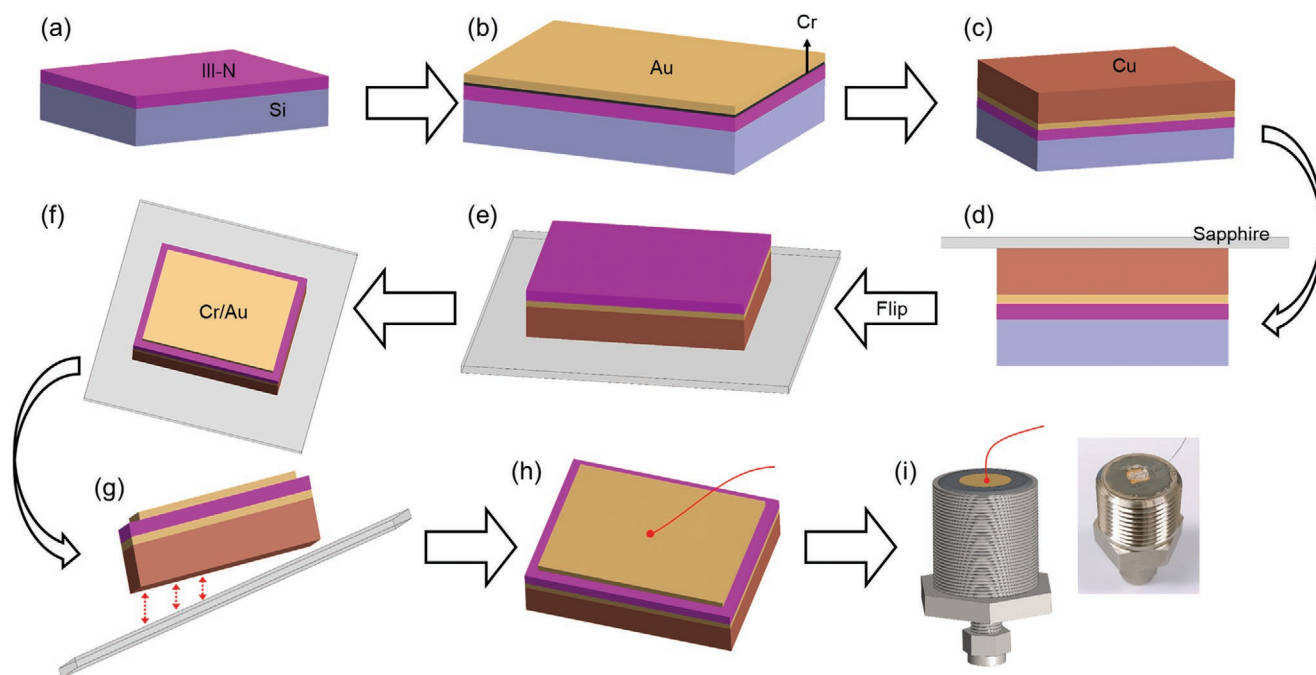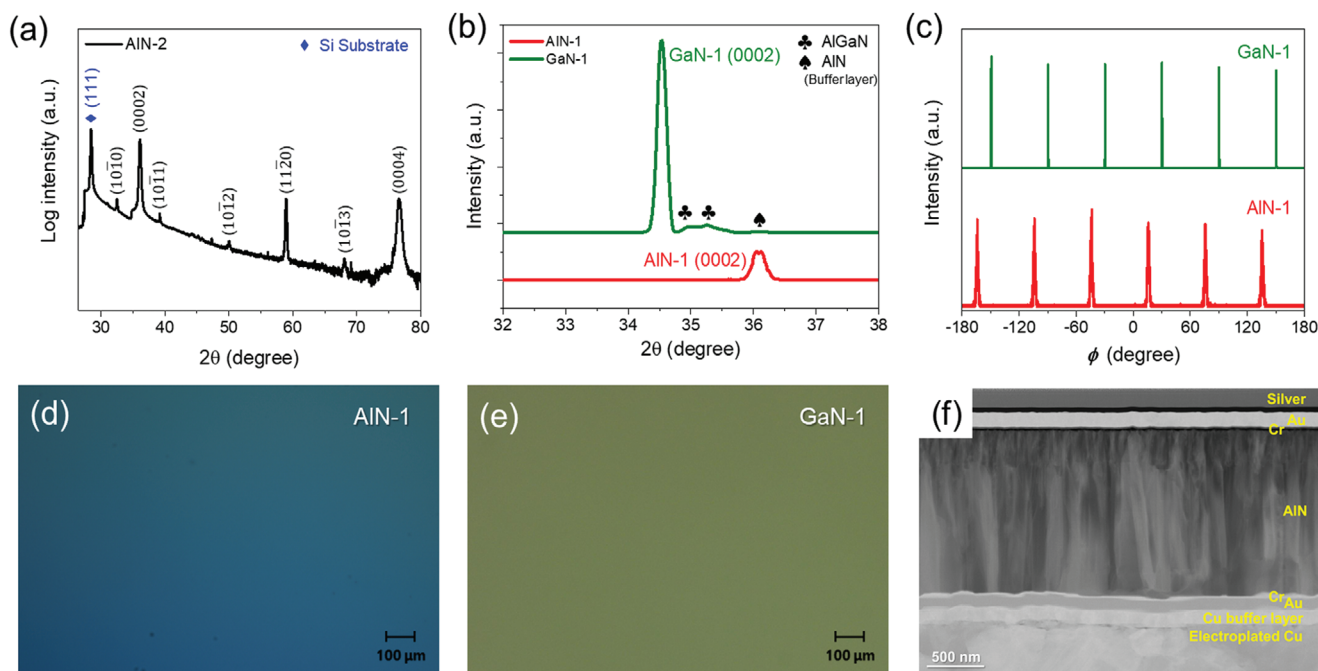
Figure 1. Schematic illustration of sensor fabrication process. a) epitaxial growth of III-N film on Si substrate, b) adhesion layer (Cr) and bottom electrode (Au) deposition, c) flexible mechanical-supporting layer deposition, d) bond to temporary handling substrate, e) Si substrate removal, f) top electrode deposition, g) handing substrate removal, h) wiring to sensor, and i) sensor module. Right photo shows an actual image of sensor module with transducer mounted on a diaphragm.

transducer, diaphragm, and tube fitting. Stainless steel foil (as a diaphragm) was laser-welded on the top side of 1-inch NPT (national pipe taper) male fitting also made of 316 stainless steel. The transducer with electrodes was attached to the diaphragm. This structure provides a compact sealing that isolates the sensor from the high-pressure hazardous or corrosive medium. The other side of fitting can be designed depending on the applications. We used 1/4-inch tube compression fitting for easy connection with a gas cylinder for pressure tests. When the pressure is applied through the tube fitting, the piezoelectric transducer experiences bending as a result of elastic deformation of the diaphragm. A schematic structure

of the sensor only with layers thicker than 1 µm, i.e., Cu and III-N films, is shown in Figure 2b. The III-N layer experiences one type of strain if the neutral plane is located in the flexible substrate, which is usually the case when the flexible substrate is significantly thicker than the III-N layer and elastic moduli are not significantly different.[15] A convex bending induces in-plane biaxial tensile strain (and resulting axial compressive strain) in the III-N film, as a neutral plane of the bent structure (transducer and Cu) is located in a relatively thick Cu supporting layer. Therefore, the applied pressure induces an axial piezoelectric polarization change in the transducer, producing an output voltage corresponding to the change of charge. The
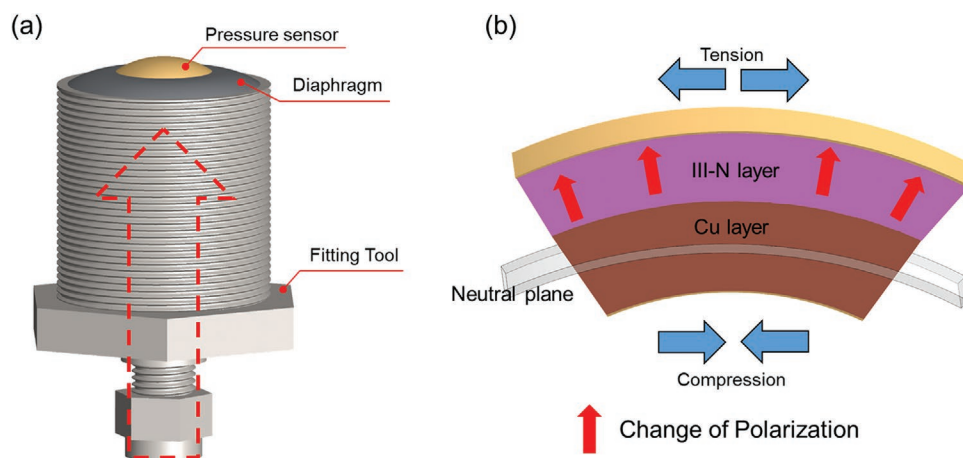
Figure 2. Schematic illustration of structure and operation of sensor module. a) Diaphragm and transducer bending in a pressurizing condition and b) piezoelectric polarization change by bending of III-N film on Cu substrate.

ADVANCED
SCIENCE NEWS
www.advancedsciencenews.com

ADVANCED
FUNCTIONAL
MATERIALS
www.afm-journal.de

Figure 3. Crystalline, surface, and structural characteristics of AlN-1, AlN-2, and GaN-1 thin films grown on Si (111) substrate. a) XRD 2θ-ω scan of AlN-2 sample, b) XRD 2θ-ω scan of AlN-1 and GaN-1 samples and c) XRD ϕ scan of AlN-1 and GaN-1 samples around $(10\bar{1}2)$ planes, optical microscope images of d) AlN-1 and e) GaN-1 thin-film surfaces, and f) cross sectional TEM image of AlN-1 sensor.

diaphragm becomes flat when the pressure is released. A concave bending by a vacuum condition will induce the voltage outputs with an opposite sign. Experimental procedures of film deposition and transducer fabrication are described in the following sections.

2.2. Crystalline and Surface Characteristics of III-N Thin Films

Figure 3 shows the characterization data by X-Ray diffraction (XRD) and optical microscopy. Figure 3a shows the XRD 2θ-ω scan of AlN-2 film containing many diffraction peaks from AlN planes. A Si peak is from (111) plane corresponding to the single-crystalline substrate with <111> orientation. However, AlN peaks are from the domains with various orientations. Besides the (0002) and (0004) peaks, the peaks from other planes are also present, including $(10\bar{1}0)$, $(10\bar{1}1)$, $(10\bar{1}2)$, $(11\bar{2}0)$, and $(10\bar{1}3)$.[16] While the crystallographic planes normal to the c-axis appear to be dominant, the epitaxial film of the AlN-2 sample possesses polycrystalline nature, possibly due to less optimized growth conditions for strain-management buffer layers in metalorganic chemical vapor deposition (MOCVD). The crystallinity of AlN remains the same after the layer transfer to a flexible substrate, showing similar multiple peaks from AlN (Figure S2, Supporting Information), which was also observed in the previous study.[17]

In contrast, epitaxial films of AlN-1 and GaN-1 samples show single-crystalline properties from the XRD. The peaks of the films only show c-axis-related planes in 2θ-ω scans. Figure 3b shows the scan range near (0002) peaks. The GaN-1 sample also shows the low-intensity peaks from AlN and two AlGaN layers which were used for strain-managed buffer layers. The thin films are epitaxially grown along the [0001] direction, i.e., the c-axis of the wurtzite structure where strong electric polarization is aligned. The peak intensity of AlN (0002) of AlN-1 sample is relatively smaller than that of GaN (0002) of GaN-1 sample. The difference is possibly due to differences in material quality and thickness–thinner AlN with compromised crystalline quality. Nevertheless, both the AlN-1 and GaN-1 layers show six strong peaks at every 60° in rotational scan (ϕ scan) around $(10\bar{1}2)$ planes (Figure 3c), clearly indicating in-plane alignment of the hexagonal lattice structure. Perfect alignments in both in-plane and out-of-plane represent the single-crystallinity of the films. The single-crystalline material without grain boundary is critical for reducing leakage between the electrodes and therefore improving the sensitivity of the sensors.[13d] The AlN-2 layer does not show peaks from the same ϕ scan. The linewidth of the peaks from AlN-1 layer is wider than that of GaN-1 layer, again suggesting compromised material quality, possibly originating from low growth temperature by physical vapor deposition techniques used for the AlN-1 sample prior to the MBE growth.

The linewidth of the peaks in rocking curves (ω scan) of symmetric and asymmetric planes is commonly used to estimate the density of threading dislocations.[18] From the full width at half maximum (FWHM) values of (0002) and $(10\bar{1}2)$ rocking curves (shown in Figure S3, Supporting Information), the densities of threading dislocations are calculated to be 2.88×10^9 and 1.58×10^{10} cm^{-2} for GaN-1 and AlN-1 layers, respectively. The density of line defects is higher for AlN-1 layer by one order of magnitude. Figure 3d,e show the microscopic images of AlN-1 and GaN-1 surfaces, respectively. Both surfaces are specular as expected from the single-crystalline film. Also, surface defects such as cracks or pinholes, which could act as a leakage

**ADVANCED
SCIENCE NEWS**

www.advancedsciencenews.com

**ADVANCED
FUNCTIONAL
MATERIALS**

www.afm-journal.de

Table 1. Comparison of transducer materials used in this study.

Sample	Crystalline quality	Thickness
GaN-1	Single-crystalline	≈3 µm
AlN-1	Single-crystalline	≈1.5 µm
AlN-2	Polycrystalline	≈2 µm

source in d_{33} mode operation, are not observed. Figure 3f is a cross sectional transmission electron microscope (TEM) image of AlN-1 sample after the device fabrication showing a structure with vertically stacked layers of electrodes and a piezoelectric transducer. It also shows rather high-density crystalline defects in the AlN layer which is in line with the results from XRD characterization (Figure S3a,b, Supporting Information). **Table 1** summarizes the crystalline quality and thickness of the transducer materials used in this study.
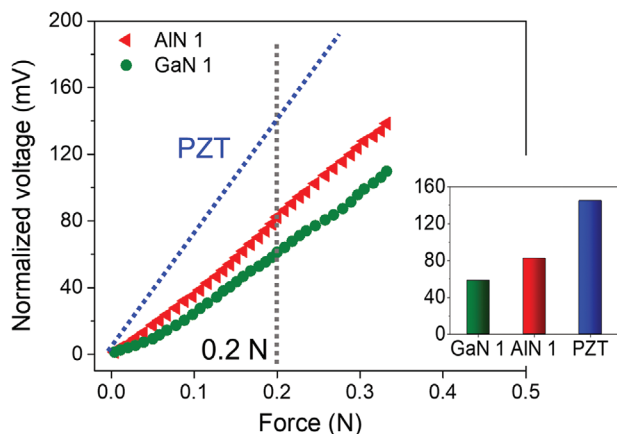
2.3. Fundamental Piezoelectric Characteristics of III-N Thin Films

Figure 4 shows normalized voltage output versus force for different piezoelectric thin films using a custom-made tester (Figure S4, Supporting Information). More applied force to the sensor means higher deflection and higher generated voltage by the sensor.[19] The results are normalized by the thickness of the thin films (2 µm), as the output voltage depends on the film thickness:

$$V_{OC} = \frac{e}{\varepsilon} x t \tag{3}$$

where V_{OC} is the open circuit voltage, x is the applied strain, and t is the thickness of piezoelectric films. Higher voltage is obtained from a thicker piezoelectric film; however, the mechanical flexibility is limited in thicker inorganic films.

Comparing the voltages at a fixed force (e.g., 0.2 N), PZT and AlN-1 and GaN-1 films show the normalized voltage of 144.8,

Figure 4. Basic piezoelectric characteristics of single-crystalline III-N thin films in comparison to that of PZT film. Electrical response with applied force. Inset shows the comparison of normalized voltages at the same force (0.2 N).

82.3, and 61.4 mV, respectively. In addition, the sensitivity of the sensor is related to the gradient of normalized voltage versus force, which are 724.1, 411.3, and 306.8 mV N⁻¹ for PZT, AlN-1, and GaN-1 films, respectively. The output voltages and sensitivity of PZT are only approximately two times higher than those of single-crystalline AlN-1 and GaN-1 layers, resulting from different ratios of the piezoelectric coefficient to dielectric constant. While the piezoelectric coefficients of PZT (e.g., e_{33} = ≈650 pC N⁻¹) are significantly higher than those of AlN (e.g., e_{33} = 5.15 pC N⁻¹), the dielectric constant of PZT (ε = 950) is also significantly higher than that of AlN (ε = 9.14).

The calculated e/ε are 0.68 and 0.56 for PZT and AlN, respectively, which indicates AlN can generate slightly lower output. However, the difference in the measured output voltages of PZT and AlN-1 layer is larger than the estimated e/ε difference. Furthermore, comparing AlN-1 and GaN-1 films, e/ε ratio of GaN-1 is 0.29, which means AlN-1 sensor should be capable to generate ≈1.9 times higher output than that of GaN-1 sensor. However, the ratio of outputs from the thickness-normalized voltages is ≈1.34. The lower output and sensitivity than expected from the AlN-1 film may be attributed to the less perfect crystalline quality of the film including the higher threshold dislocation density (Figure S3a,b, Supporting Information). The high-resolution TEM image (Figure S3c, Supporting Information) shows each atom is well-matched with the schematic atomic structure. Further improvement in the crystalline quality of AlN thin film is needed to enhance the sensitivity comparable to that of PZT.

The output characteristics of AlN-1 sensor were further tested by subjecting it to a cyclic 0.1 N force (loading and releasing) for 60 min. Under long-term periodic deflection, the AlN-1 sensor displays a repeated waveform with no trace of degradation in the electrical output (Figure S5, Supporting Information). The device shows excellent durability due to its piezoelectric working mechanism. Additionally, Figure S5b (Supporting Information) which is the zoom-in signal of electrical response at various time intervals, reveals that the AlN sensor exhibits excellent repeatability since the output voltage variation in each recorded time and time interval is less than 0.1 mV.

Figure 5a demonstrates the simulated stress profile of AlN thin film sensor on a diaphragm. The diaphragm and AlN sensor are gradually distorted (shown by color contour) as the applied gas pressure increases with stress levels of 0.38, 0.695, 1.04, and 1.353 ($\times 10^6$ N m⁻²) for input gas pressures of 50, 100, 150, and 200 psi, respectively. The simulated output voltage increases accordingly from 39 to 135 mV for pressure from 50 to 200 psi (Figure 5b).

2.4. Output Voltage Characteristics in Extreme Environment

In order to provide an extreme environment for the III-N thin film-based sensor module, a tube furnace system including an electric temperature controller was used together with a nitrogen gas tube and a pressurizing regulator (Figure S6, Supporting Information).

Figure 6 shows the measured voltages and calculated sensitivity of AlN-1, AlN-2, and GaN-1 sensors as a function of temperature and applied pressure. Output voltage at a fixed
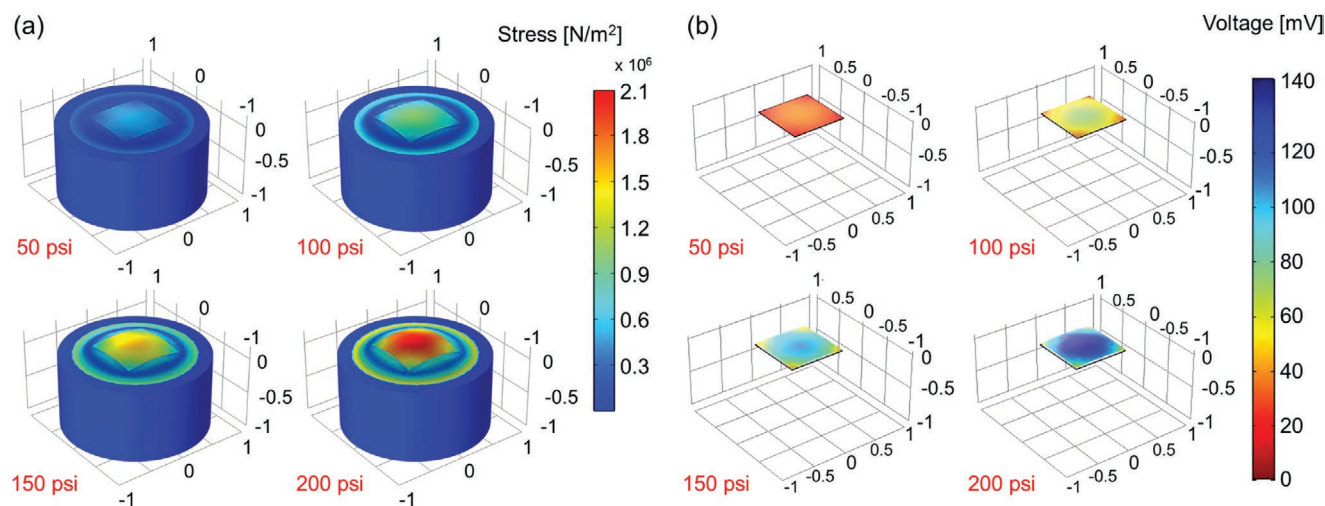
Figure 5. Simulated stress and piezoelectric output of AlN sensor. a) Stresses acting on diaphragm and b) corresponding output voltages generated by gas pressures at 50, 100, 150, and 200 psi.

pressure is affected by temperature. Figure 6a,b,c show that the output voltages of the AlN-1, GaN-1, and, AlN-2 sensors, respectively, at a constant pressure increase up to a certain temperature and then decrease. The maximum output values were obtained at 800, 300, and 600 °C for AlN-1, GaN-1, and AlN-2 sensors, respectively. Highlighted areas of output voltages from Figure 6a,b are displayed in Figure 6d,e as a function of pressure in each temperature range. For AlN-1 sensor at room temperature, the output voltage increases from 38.7 to 66.8, 86.3,

and 106.1 mV for an input pressure of 50, 100, 150, and 200 psi, respectively, which are closely matched with simulated output values (Figure 5b). All the sensors are fully functional up to high pressure of 200 psi and we expect higher pressure operation as long as the stainless-steel diaphragm is deformed elastically. Comparing the sensors at the same temperatures of less than 300 °C, the output voltages of GaN-1 sensor are slightly higher than those of AlN-1 sensor due to the difference in thickness: thinner AlN-1 film (≈1.5 μm) than GaN-1 film (≈3 μm).
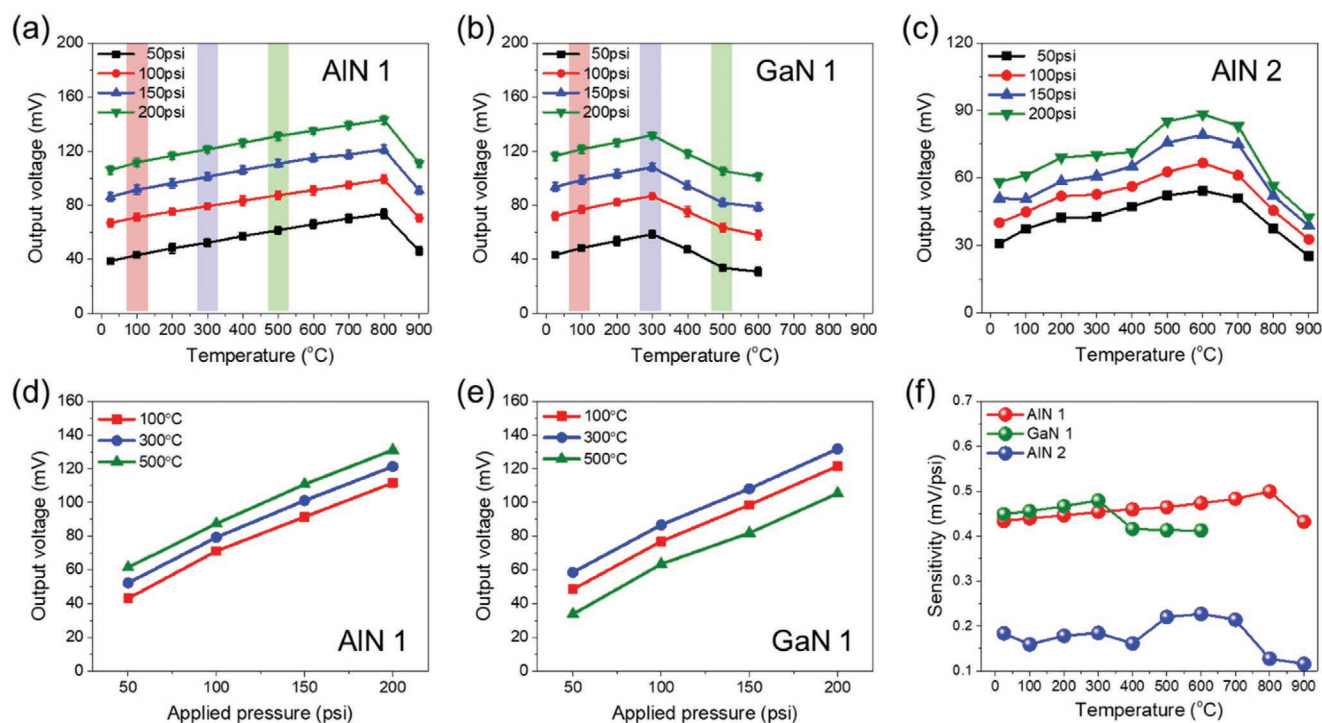
Figure 6. Sensor output characteristics at different pressures and temperatures. Output voltage as a function of temperature at different pressures from a) AlN-1, b) GaN, and c) AlN-2 sensors. Output voltage as a function of pressure at different temperatures from d) AlN-1 and e) GaN-1. f) Sensitivity as a function of temperature of different sensors.

ADVANCED
SCIENCE NEWS
www.advancedsciencenews.com

ADVANCED
FUNCTIONAL
MATERIALS
www.afm-journal.de

The output voltages of AlN-2 sensor are significantly lower than those of AlN-1 and GaN-1 sensors because of its polycrystalline film containing different orientations of grains and grain boundaries from Figure 3a and Figure S2 (Supporting Information).

The temperatures with the maximum output values indicate the highest sensitivity for these sensors (Figure 6f), even though, the sensors are still functional beyond these temperatures with lower sensitivity. This temperature-dependent sensitivity is further investigated in the following section. Also, the sensitivity is not only low but also not following a trend. It is clear that single-crystallinity plays an important role in sensor sensitivity. Moreover, AlN-1 sensor shows higher sensitivity than GaN-1 sensor at a temperature range beyond 300 °C, due to its wider bandgap.

The performance characteristics of the sensors need to be stable and reliable for real applications. In order to investigate stability and reliability, the III-N pressure sensor was measured over a long period of time in the same manner as the measurement in Figure 6. When measured at constant pressure for a long time (e.g., 600 s) at a constant temperature (e.g., 300 °C), the AlN-1 sensor does not show any change in the output voltage as exhibited in Figure S7 (Supporting Information). This suggests that no leakage occurs between two electrodes in a long operating time and stable and reliable measurement can be achieved from these III-N sensors. Additionally, sharp increase and decrease are measured upon pressurizing and venting, respectively, indicating the fast response of the III-N sensors (≈4 ms).

2.5. Temperature-Dependent Output Voltage Characteristics

The origins of the temperature dependence of output voltages have to be studied for accurate sensor calibration in our study. First, the increase in voltage may be related to the temperature-dependent elastic modulus. The modulus of elasticity generally decreases with temperature. Among the materials used in the sensor module, we only consider stainless steel which is the material of the diaphragm. **Figure 7**a shows the elastic modulus of stainless steel inversely proportional to temperature.[20] Thus, the diaphragm and mounted sensor become more deformed under identical pressure when the temperature is raised and our simulation using COMSOL software shows that higher output voltage is measured from the sensors in whole temperature range for AlN and GaN (Figure S8, Supporting Information).

On the other hand, output voltages start decreasing at ≈800 and ≈300 °C for AlN-1 and GaN-1 sensors, respectively due to the significant generation of intrinsic charge carriers.[14] The temperature effect in AlN-2 sensor is not considered because it shows low sensitivity and influence from grain boundaries. The intrinsic carrier concentration of a semiconductor, n_i is a strong function of a ratio of bandgap energy to temperature:

$$n_i = \sqrt{N_c N_v} \exp\left(\frac{-E_g}{2k_B T}\right) \qquad (4)$$

where N_c is the effective density of states of the conduction band ($1.2 \times 10^{15} \times T^{3/2}$ and $4.3 \times 10^{14} \times T^{3/2}$ cm^{-3} for wurtzite crystal structure of AlN and GaN, respectively), N_v is the effective density of states of the valence band ($9.4 \times 10^{16} \times T^{3/2}$ and $8.9 \times 10^{15} \times T^{3/2}$ cm^{-3} for AlN and GaN, respectively),[21] E_g is the bandgap energy, k_B is the Boltzmann constant, and T is temperature. Temperature-dependent bandgap energy is also considered by Varshni's equation:

$$E_g = E_g(0) - \frac{\gamma T^2}{T + \beta} \qquad (5)$$

where E_g (0) is bandgap energy at 0 K (3.47 and 6.23 eV for GaN and AlN, respectively), γ is an empirical constant (0.77 and 1.799 mV K^{-1} for GaN and AlN, respectively) and β is associated with the Debye temperature of the crystal (600 and 1462 K for GaN and AlN, respectively).[22] Figure 7b shows the intrinsic carrier concentration of AlN and GaN. The concentrations remain nearly the same (on the order of 10^7 cm^{-3}) and then significantly increase at 800 and 300 °C for AlN and GaN, respectively. Piezoelectric properties are partially screened by free carriers.[23] In typical unintentionally doped semiconductors where free carriers from doping are negligible, the free carriers are generated by thermal excitation from band-to-band transition, which occurs at higher temperatures for wider bandgap materials. In the previous study from the GaN sensor, decreasing output voltage beyond ≈300 °C was observed, possibly due to increasing concentrations of free carriers.[14]
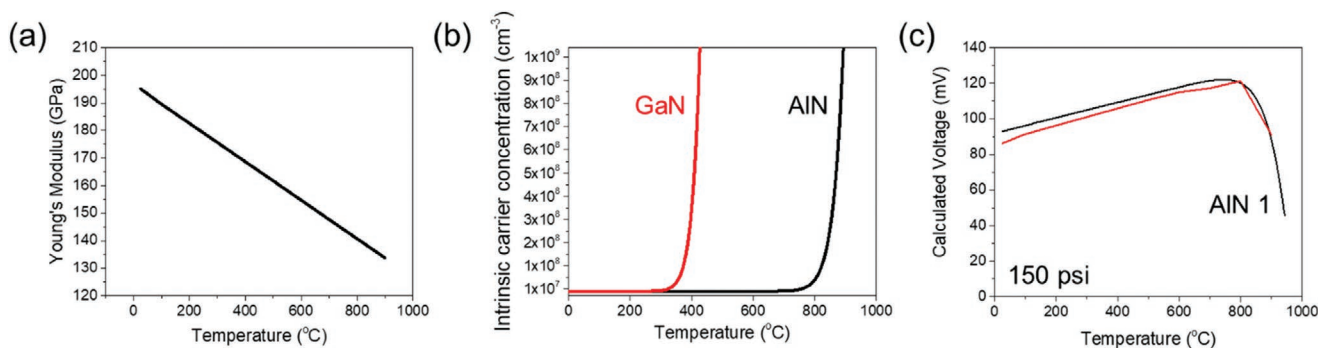
Figure 7. a) Elastic modulus of stainless steel as a function of temperature. b) Calculated intrinsic carrier concentration of AlN and GaN as a function of temperature. c) Calculated and experimented output voltage of AlN-1 sensor as a function of temperature at 150 psi considering the effects of elastic modulus change of diaphragm and the screening of piezoelectricity by free carriers.

Therefore, besides the development of an AlN-based sensor, temperature-dependent sensor characteristics between GaN and AlN are compared.

A nonlinear Poisson equation is solved to further investigate the screening effect by free carriers on the piezoelectric potential. The equation characterizes the relationship between total charge distribution and potential:[24]

$$k_{ik} \frac{\partial^2}{\partial x_i \, \partial x_k} \varphi = -(\rho^{\text{deformed}} - e n_i) \tag{6}$$

where k_{ik} is the relative dielectric constant in ik direction that is simplified to k_{33} in this case (9.14 and 9.5 for AlN and GaN, respectively), φ is piezoelectric potential, and ρ^{deformed} is the piezoelectric charge generated by deformation. The contributions from ionized donors and acceptors are ignored in this study for unintentionally doped materials. The voltage decreases corresponding to increasing carrier concentration (Figure S9, Supporting Information). The effects of elastic modulus change in the diaphragm and free-carrier screening are combined and representatively shown in Figure 7c for AlN-1 sensor at 150 psi. The calculated changes at other pressure are shown in Figure S10 (Supporting Information). The comparison between the calculation and experiment clearly supports that the sensitivity of AlN-1 sensor first increases by elastic modulus change of the diaphragm and then decreases by free carrier generation. The piezoelectric potential suppression of AlN-1 sensor occurs at very high temperatures (> 800 °C) due to its ultrawide bandgap, making it a promising candidate for high-temperature applications.

3. Conclusion

In summary, we fabricated, characterized, and analyzed flexible pressure sensors made of wide-bandgap piezoelectric III-N layers epitaxially grown by chemical vapor deposition and physical vapor deposition followed by thin-film layer transfer. X-ray diffraction examination revealed the single-crystalline wurtzite structure for AlN-1 and GaN-1 films and non-single crystallinity for AlN-2 films. The output voltages of these III-N-based pressure sensors were experimentally measured and theoretically studied in which these values were in good agreement. The electrical response of AlN-1 and GaN-1 sensors with respect to applied force at room temperature revealed higher normalized output voltage for AlN-1 sensors with excellent stability and repeatability over 0.1 N periodic force for 60 min. AlN-1, AlN-2, and GaN-1 pressure sensors were tested up to 900 °C and 200 psi. Their output voltages were increased by applying more pressure at a constant temperature due to more deformation in the diaphragm and sensors themselves. The sensors were functional beyond 200 psi as long as the stainless-steel diaphragm shows elastic behavior. The output voltages of the AlN-1 and GaN-1 sensors were first increased with temperature up to a particular temperature (800 and 300 °C, respectively) by the softening of the diaphragm, and then started to decrease due to intrinsic carrier generation in their thin films. Beyond these temperatures, the sensors are still operational but with lower sensitivity. These results were also confirmed theoretically. The

long-term stability at 300 °C for various pressure levels was also examined and demonstrated fast, stable, and reliable measurements. The piezoelectric flexible single-crystalline AlN pressure sensor was demonstrated as the highest operating temperature sensor ever demonstrated and is particularly promising for high-pressure and high-temperature applications in harsh environments over extended periods.

4. Experimental Section

III-N Thin-Film Deposition: Three III-N thin films were prepared as transducers having different bandgap energies and crystalline quality. All the layers were grown on Si (111) substrates for the use of an economical substrate and easy implementation of a layer-transfer process (refer to Section 2.1. Design of flexible sensor and sensor module). For a comparison with AlN samples, a single-crystalline GaN film was epitaxially grown by MOCVD employing $Al_xGa_{1-x}N$ buffer layers (sample GaN-1). The total thickness of the film was ≈3 µm including buffer layers (≈1 µm). A single-crystalline AlN film was deposited by DC magnetron sputtering followed by molecular-beam epitaxy (MBE) (sample AlN-1), to avoid the problem of epitaxial growth of AlN thin film on Si substrate by MOCVD, e.g., crack formation due to significant difference in the thermal expansion coefficients and lattice mismatch between AlN and Si (111).[25] While the film was a single-crystalline film free of cracks, the crystalline quality of the film was compromised due to the epitaxial growth by physical vapor deposition at relatively lower temperatures. The total thickness of the AlN film was ≈1.5 µm. Another AlN sample with a thickness of ≈2 µm was grown by MOCVD using thermal-expansion-mitigated buffer layers (sample AlN-2). Due to the less optimized buffer conditions, the AlN layer was not single-crystalline.

Device Packaging: Now the III-N sensor was mechanically flexible and ready to be mounted on the diaphragm. To ensure leak tightness, the stainless-steel diaphragm with a thickness of 100 µm was laser-welded onto the round face of the NPT fitting. The diaphragm was then coated with silver paste (Ted Pella) to lower the contact resistance between the sensor and the diaphragm. The fabricated flexible sensor was bonded to the diaphragm, and the surface of the Cu and diaphragm were coated with high-temperature glue before being left at room temperature for 10 h to solidify. The wire was also joined with silver paste on the top electrode, and the middle of the wire was covered with high-temperature adhesive to avoid separation.

Materials Characterization: The crystalline structure and quality of III-N thin films were studied by high-resolution X-ray diffraction (HR-XRD) (Bruker, D8 Discover system) and high-resolution transmission electron microscopy (Thermo Fisher Scientific, FEI Titan Themis Z). The crystallinity, defect, and level of alignments of the III-N crystals were investigated using a variety of XRD scans. Additionally, to detect the existence of cracking or other surface imperfections of the III-N sensor, a digital optical microscope (Keyence, VHX-600) was used.

Piezoelectric Characteristics Measurement and Modeling: Electromechanical properties of piezoelectric thin films were characterized quantitatively by a custom-made tester (schematically shown in Figure S4, Supporting Information) in which thin films underwent a periodic deflection by a micrometer drive which was controlled by a motor. The real-time output voltage of thin films was recorded for various applied forces generated by the micrometer drive. COMSOL Multiphysics software was used to conduct numerical modeling to simulate the output voltages from the sensor with varied pressure conditions. A flexible AlN thin-film layer on a stainless-steel diaphragm was used in the model.

High-Temperature Measurement: For high-temperature measurements (schematically shown in Figure S6, Supporting Information), the III-N sensors were operated in a tube furnace from 100 to 900 °C with an increment of 100 °C. The temperature of the furnace was changed and the heating rate was fixed as 10 °C min⁻¹. Data were collected by keeping

the furnace at a constant temperature and measuring the output voltage at various pressures. Pressure-regulated nitrogen (N_2) gas was used to evaluate the pressure-sensing characteristics. To manage the target pressures, an N_2 gas cylinder was attached to a regulator (50, 100, 150, and 200 lb in^{-2}, psi). High-pressure N_2 was connected to the sensor housing through 1/4 tube. For regulated gas input and release, two valves were also fitted to pressurize and exhaust the sensor housing. A gas regulator was used to regulate the gas pressure. To pressurize the pipe with N_2 gas, the inlet valve was opened and subsequently closed. The outlet valve was then opened to evacuate the pipe while the output voltages of the sensor were measured. To ensure the validity of output voltages, this method was repeated. Computer software (LabView) with an electrometer (Keithley, 6514) recorded the output voltages of the sensor.

Supporting Information

Acknowledgements

Conflict of Interest

The authors declare no conflict of interest.

Data Availability Statement

The data that support the findings of this study are available from the corresponding author upon reasonable request.

Keywords

[1] a) G. O. Fridleifsson, W. A. Elders, *Geothermics* **2005**, *34*, 269; b) G. H. Kroetz, M. H. Eickhoff, H. Moeller, *Sens. Actuators, A* **1999**, *74*, 182; c) C. Soares, *Gas Turbines*, 2nd ed., Butterworth-Heinemann, Oxford **2015**; d) Y. Javed, M. Mansoor, I. A. Shah, *Sens. Rev.* **2019**, *39*, 652; e) J. Čížek, J. Kalivodová, M. Janeček, J. Stráský, O. Srba, A. Macková, *Metals* **2021**, *11*, 76.

[2] a) J. von Berg, R. Ziermann, W. Reichert, E. Obermeier, M. Eickhoff, G. Krötz, U. Thoma, T. Boltshauser, C. Cavalloni, J. P. Nendza, *Mater. Sci. Forum* **1997**, *264–268*, 1101; b) J. v. Berg, R. Ziermann, W. Reichert, E. Obermeier, M. Eickhoff, G. Krotz, U. Thoma, C. Cavalloni, J. P. Nendza, in Fourth Int. High Temp. Electron. Conf. HITEC (Cat. No.98EX145), IEEE, Piscataway, NJ **1998**.

[3] A. A. Ned, R. S. Okojie, A. D. Kurtz, in Fourth Int. High Temp. Electron. Conf. HITEC (Cat. No.98EX145), IEEE, Piscataway, NJ **1998**.

[4] a) Z. Lian, Y. JinSong, L. Hao, in 2011 6th IEEE Conf. Ind. Electron. Appl., IEEE, Piscataway, NJ **2011**; b) K. Kasten, J. Amelung, W. Mokwa, *Sens. Actuators A* **2000**, *85*, 147.

[5] N. A. Riza, M. Sheikh, F. Perez, *J. Eng. Gas Turbines Power* **2010**, *132*, 051601.

[6] a) S. Roundy, P. K. Wright, *Smart Mater. Struct.* **2004**, *13*, 1131; b) J. Luo, L. Zhang, T. Wu, H. Song, C. Tang, *Extreme Mech Lett* **2021**, *48*, 101279; c) R. J. Brook, *Concise Encyclopedia of Advanced Ceramic Materials*, Elsevier, Oxford **2012**; d) K. Uchino, *Advanced Piezoelectric Materials*, Woodhead Publishing, Cambridge, England **2017**.

[7] a) R. C. Turner, P. A. Fuierer, R. E. Newnham, T. R. Shrout, *Appl. Acoust.* **1994**, *41*, 299; b) H. Fritze, *J Electroceram* **2006**, *17*, 625.

[8] a) J. Hornsteiner, E. Born, G. Fischerauer, E. Riha, in Proc. 1998 IEEE Int. Freq. Control Symp. (Cat. No.98CH36165), IEEE, Piscataway, NJ **1998**; b) K. Lucas, S. Bouchy, P. Bélanger, R. J. Zednik, *J. Appl. Phys.* **2022**, *131*, 194102.

[9] a) H. Fritze, H. Seh, H. L. Tuller, G. Borchardt, *J. Eur. Ceram. Soc.* **2001**, *21*, 1473; b) H. Fritze, H. L. Tuller, *Appl. Phys. Lett.* **2001**, *78*, 976; c) D. Damjanovic, *Curr Opin Solid State Mater Sci* **1998**, *3*, 469; d) J. Haines, O. Cambon, D. A. Keen, M. G. Tucker, M. T. Dove, *Appl. Phys. Lett.* **2002**, *81*, 2968.

[10] S. O. Leontsev, R. E. Eitel, *Sci. Technol. Adv. Mater.* **2010**, *11*, 044302.

[11] a) T. L. Chu, *J. Electrochem. Soc.* **1971**, *118*, 1200; b) M. Stutzmann, O. Ambacher, A. Cros, M. S. Brandt, H. Angerer, R. Dimitrov, N. Reinacher, T. Metzger, R. Höpler, D. Brunner, F. Freudenberg, R. Handschuh, C. Deger, *Mater. Sci. Eng., B* **1997**, *50*, 212; c) P. G. Neudeck, R. S. Okojie, C. Liang-Yu, *Proc. IEEE* **2002**, *90*, 1065; d) C. Besleaga, V. Dumitru, L. M. Trinca, A.-C. Popa, C.-C. Negrila, Ł. Kołodziejczyk, C.-R. Luculescu, G.-C. Ionescu, R.-G. Ripeanu, A. Vladescu, G. E. Stan, in *Nanomaterials*, 394, 7, **2017**.

[12] S. A. Jewett, M. S. Makowski, B. Andrews, M. J. Manfra, A. Ivanisevic, *Acta Biomater.* **2012**, *8*, 728.

[13] a) J. Chen, N. Nabulsi, W. Wang, J. Y. Kim, M.-K. Kwon, J.-H. Ryou, *Appl. Energy* **2019**, *255*, 113856; b) J. Chen, H. Liu, W. Wang, N. Nabulsi, W. Zhao, J. Y. Kim, M.-K. Kwon, J.-H. Ryou, *Adv. Funct. Mater.* **2019**, *29*, 1903162; c) J. Chen, S. K. Oh, N. Nabulsi, H. Johnson, W. Wang, J.-H. Ryou, *Nano Energy* **2019**, *57*, 670; d) N.-I. Kim, J. Chen, W. Wang, M. Moradnia, S. Pouladi, M.-K. Kwon, J.-Y. Kim, X. Li, J.-H. Ryou, *Adv. Funct. Mater.* **2021**, *31*, 2008242.

[14] N.-I. Kim, Y.-L. Chang, J. Chen, T. Barbee, W. Wang, J.-Y. Kim, M.-K. Kwon, S. Shervin, M. Moradnia, S. Pouladi, D. Khatiwada, V. Selvamanickam, J.-H. Ryou, *Sens. Actuators, A* **2020**, *305*, 111940.

[15] a) S. Shervin, S.-H. Kim, M. Asadirad, S. Ravipati, K.-H. Lee, K. Bulashevich, J.-H. Ryou, *Appl. Phys. Lett.* **2015**, *107*, 193504; b) W. Wang, J. Chen, J. S. Lundh, S. Shervin, S. K. Oh, S. Pouladi, Z. Rao, J. Y. Kim, M.-K. Kwon, X. Li, S. Choi, J.-H. Ryou, *Appl. Phys. Lett.* **2020**, *116*, 123501.

[16] a) G. A. Jeffrey, G. S. Parry, R. L. Mozzi, *J. Chem. Phys.* **1956**, *25*, 1024; b) E. Ruiz, S. Alvarez, P. Alemany, *Phys. Rev. B* **1994**, *49*, 7115.

[17] J. Chen, S. K. Oh, H. Zou, S. Shervin, W. Wang, S. Pouladi, Y. Zi, Z. L. Wang, J.-H. Ryou, *ACS Appl. Mater. Interfaces* **2018**, *10*, 12839.

[18] a) P. Gay, P. B. Hirsch, A. Kelly, *Acta Metall.* **1953**, *1*, 315; b) V. M. Kaganer, O. Brandt, A. Trampert, K. H. Ploog, *Phys. Rev. B* **2005**, *72*, 045423.

[19] N.-I. Kim, J. M. Lee, M. Moradnia, J. Chen, S. Pouladi, M. Yarali, J. Y. Kim, M.-K. Kwon, T. R. Lee, J.-H. Ryou, *Soft Sci.* **2022**, *2*, 8.

[20] a) T. S. Byun, N. Hashimoto, K. Farrell, *Acta Mater.* **2004**, *52*, 3889; b) B. G. Kim, J. L. Rempe, D. L. Knudson, K. G. Condie, B. H. Sencer, *Nucl. Technol.* **2012**, *179*, 417.

[21] M. E. Levinshtein, S. L. Rumyantsev, M. S. Shur, *Properties of Advanced Semiconductor Materials: GaN, AlN, InN, BN, SiC, SiGe*, John Wiley & Sons, Nashville, TN **2001**.

[22] I. Vurgaftman, J. R. Meyer, L. R. Ram-Mohan, *J. Appl. Phys.* **2001**, *89*, 5815.

[23] a) X. Xue, Y. Nie, B. He, L. Xing, Y. Zhang, Z. L. Wang, *Nanotechnology* **2013**, *24*, 225501; b) C.-H. Wang, W.-S. Liao, N.-J. Ku, Y.-C. Li, Y.-C. Chen, L.-W. Tu, C.-P. Liu, *Small* **2014**, *10*, 4718.

[24] T. T. Pham, K. Y. Lee, J.-H. Lee, K.-H. Kim, K.-S. Shin, M. K. Gupta, B. Kumar, S.-W. Kim, *Energy Environ. Sci.* **2013**, *6*, 841.

[25] W. M. Yim, R. J. Paff, *J. Appl. Phys.* **1974**, *45*, 1456.